Inhibition of nucleotide synthesis promotes replicative senescence of human mammary epithelial cells

Received for publication, September 21, 2018, and in revised form, May 18, 2019 Published, Papers in Press, May 28, 2019, DOI 10.1074/jbc.RA118.005806

Alireza Delfarah[‡], Sydney Parrish[‡], Jason A. Junge[§], Jesse Yang[‡], Frances Seo[‡], Si Li[‡], John Mac[‡], Pin Wang[‡], Scott E. Fraser[§], and Nicholas A. Graham[‡¶1]

From the [‡]Mork Family Department of Chemical Engineering and Materials Science, the [§]Translational Imaging Center, Molecular and Computational Biology, and the [¶]Norris Comprehensive Cancer Center, University of Southern California, Los Angeles, California 90089

Edited by Jeffrey E. Pessin

Cellular senescence is a mechanism by which cells permanently withdraw from the cell cycle in response to stresses including telomere shortening, DNA damage, or oncogenic signaling. Senescent cells contribute to both age-related degeneration and hyperplastic pathologies, including cancer. In culture, normal human epithelial cells enter senescence after a limited number of cell divisions, known as replicative senescence. Here, to investigate how metabolic pathways regulate replicative senescence, we used LC-MS–based metabolomics to analyze senescent primary human mammary epithelial cells (HMECs). We did not observe significant changes in glucose uptake or lactate secretion in senescent HMECs. However, analysis of intracellular metabolite pool sizes indicated that senescent cells exhibit depletion of metabolites from nucleotide synthesis pathways. Furthermore, stable isotope tracing with ^{13}C-labeled glucose or glutamine revealed a dramatic blockage of flux of these two metabolites into nucleotide synthesis pathways in senescent HMECs. To test whether cellular immortalization would reverse these observations, we expressed telomerase in HMECs. In addition to preventing senescence, telomerase expression maintained metabolic flux from glucose into nucleotide synthesis pathways. Finally, we investigated whether inhibition of nucleotide synthesis in proliferating HMECs is sufficient to induce senescence. In proliferating HMECs, both pharmacological and genetic inhibition of ribonucleotide reductase regulatory subunit M2 (RRM2), a rate-limiting enzyme in dNTP synthesis, induced premature senescence with concomitantly decreased metabolic flux from glucose into nucleotide synthesis. Taken together, our results suggest that nucleotide synthesis inhibition plays a causative role in the establishment of replicative senescence in HMECs.

Cellular senescence is an irreversible growth arrest that occurs in response to a variety of cellular stresses including DNA damage, oncogenic signaling, and oxidative stress (1). Senescent cells accumulate in aging tissues and contribute to age-related decline in tissue function (2–4). In culture, replicative senescence occurs in normal cells after a limited number of population doublings, the so-called Hayflick limit (5). Following activation of oncogenes including KRAS and BRAF, senescence acts to prevent proliferation, thus preventing against cancer (6–9). In addition to its role in aging and tumor suppression, senescent cells can contribute to hyperplastic pathologies including cancer through secretion of numerous pro-inflammatory signals (*i.e.* senescence-associated secretory phenotype) (10).

Although senescent cells are permanently arrested, they are highly metabolically active and demonstrate significant metabolic differences compared with proliferating, nonsenescent cells (11). Studies of human fibroblasts in culture have shown that replicative senescence is accompanied by increased glycolysis (12–14). In oncogene-induced senescence, increased glucose consumption is shunted away from the pentose phosphate pathway, leading to decreased nucleotide synthesis (6, 15, 16). Alterations in mitochondrial function can also induce senescence through 5′ AMP-activated protein kinase– and p53–dependent pathways (17, 18). Importantly, it has also been demonstrated that metabolic genes, including phosphoglycerate mutase, pyruvate dehydrogenase, and malic enzymes, can regulate entry into and escape from senescence (8, 19, 20). Therefore, identifying the mechanisms by which metabolism regulates senescence is essential to understanding the senescence program during aging and tumor suppression.

Primary human mammary epithelial cells (HMECs)[2] have been shown to exhibit two mechanistically distinct senescence barriers to immortalization: stasis and agonescence (21). Stasis is a retinoblastoma-mediated growth arrest that occurs in the absence of DNA damage and is independent of p53 (22). Agonescence, or telomere dysfunction-associated senescence, is driven by critically shortened telomeres that trigger both a p53-dependent cell cycle arrest and a DNA damage response

This work was supported by the Rose Hills Foundation, the University of Southern California (USC) Provost's Office, the USC Translational Imaging Center, and the Viterbi School of Engineering. The authors declare that they have no conflicts of interest with the contents of this article.

This article contains Tables S1–S11 and Figs. S1–S10.

[1] To whom correspondence should be addressed: University of Southern California, 3710 McClintock Ave., RTH 509, Los Angeles, CA 90089. Tel.: 213-240-0449; E-mail: nagraham@usc.edu.

[2] The abbreviations used are: HMEC, human mammary epithelial cell; CRISPRi, CRISPR-dCas9 interference; EdU, 5-ethynyl-2′-deoxyuridine; FDR, false discovery rate; GSEA, gene set expression analysis; PD, population doubling(s); RRM2, ribonucleotide reductase regulatory subunit M2; SA-β-gal, senescence-associated β-galactosidase; hTERT, human telomerase; SAHF, senescence-associated heterochromatic foci; TCA, tricarboxylic acid; PRPP, phosphoribosyl pyrophosphate; NA, numerical aperture; PAI-1, plasminogen activator inhibitor-1.

(23, 24). Because properties associated with senescence in mesenchymal cell types such as fibroblasts may not accurately reflect senescence in epithelial cells (22), the study of primary HMECs is required to understand how these senescence barriers are involved in normal HMEC biology, including aging and oncogenesis. How these senescence barriers are regulated by cellular metabolism in this primary cell type has not been investigated previously.

Here, we report that replicative senescence in primary HMECs is accompanied by a dramatic inhibition of nucleotide synthesis, including reduced flux of both glucose- and glutamine-derived carbon into nucleotide synthesis pathways. Expression of human telomerase (hTERT) in HMECs both induced immortalization and maintained flux into nucleotide synthesis. In addition, treatment of proliferating HMECs with an inhibitor of ribonucleotide reductase regulatory subunit M2 (RRM2), a key enzyme in dNTP biosynthesis, induced senescence and recapitulated the metabolomic state of replicative senescence. Taken together, our results indicate that nucleotide metabolism is a key regulator of replicative senescence in HMECs.

Results

Establishment of a human mammary epithelial cell model of senescence

To study the metabolic alterations that accompany replicative senescence, we used normal diploid HMECs. These cells have been shown previously to accurately represent the molecular changes that occur during replicative senescence *in vivo* (21). We observed linear growth for ~15 population doublings (PD), after which cell growth slowed until cells ceased proliferation at ~40 PD (Fig. 1*A*). HMECs at ~40 PD were viable and showed little to no cell death (Fig. 1*B*). However, these cells showed an enlarged, flattened, and irregular morphology that is typical of senescent cells (25) (Fig. 1*C*). To confirm that HMECs at ~40 PD were senescent, we first measured senescence-associated β-gal (SA-β-gal) activity using C_{12}FDG, a fluorogenic substrate for SA-β-gal activity in live cells (26), and observed increased SA-β-gal activity at PD 40 (Fig. 1*D*). Next, we confirmed that senescent HMECs exhibited a lack of DNA synthesis by measuring incorporation of the thymidine analog 5-ethynyl-2′-deoxyuridine (EdU) (Fig. 1*E*). Notably, Hoechst staining revealed that senescent HMECs did not exhibit senescence-associated heterochromatic foci (SAHF), a frequent but not obligatory marker of senescence (27). However, we observed that a significant fraction of senescent HMECs were multinuclear (Fig. 1*F* and Fig. S1), which has been observed in senescent human melanocyte systems (28) and can result from aberrant mitotic progression in oncogene-induced senescence (29). Next, we tested for expression of the senescence markers p16 and p21. Western blotting revealed that senescent HMECs exhibited increased expression of p21 but not p16 (Fig. 1*G*). Because SAHF formation is driven by p16 but not p21, this observation is consistent with our finding that senescent HMECs do not exhibit SAHF (27, 30). We also tested for expression of the senescence marker PAI-1 (plasminogen activator inhibitor-1) (31–33) by Western blotting and observed increased expression in senescent HMECs (Fig. 1*G*). Finally, to investigate whether senescent HMECs experienced DNA damage, we tested for expression of the DNA damage marker γ-H2AX by Western blotting. Interestingly, expression of γ-H2AX was slightly decreased as cells entered senescence (Fig. 1*H*), suggesting that senescent HMECs do not exhibit dsDNA breaks (22). Taken together, these data demonstrate that HMECs enter senescence around 35–40 PD.

Senescent HMECs do not exhibit a glycolytic shift

Having established a model system for replicative senescence, we analyzed proliferating and senescent HMECs using LC-MS–based metabolomics (34, 35). First, we measured the consumption and secretion rates of glucose and lactate, respectively (Fig. 2*A* and Table S1). Neither glucose consumption, lactate secretion, nor the ratio of glucose consumption to lactate secretion was significantly altered, suggesting that senescent HMECs do not exhibit an overall glycolytic shift. Because senescent fibroblasts increase secretion of citrate (13), we next examined the secretion of TCA cycle metabolites. Senescent HMECs exhibited decreased secretion of most TCA cycle metabolites, although only aconitate and malate demonstrated significant reductions (Fig. S2*A*). Finally, we examined the consumption and secretion of amino acids in proliferating and senescent cells. Although consumption and secretion of many amino acids was reduced in senescent HMECs, only aspartate secretion was significantly reduced compared with proliferating HMECs (Fig. S2*B*). Notably, glutamine consumption, a significant carbon source for the TCA cycle, was not significantly reduced. Taken together, these data demonstrate that senescent HMECs are highly metabolically active, without significant changes in glycolytic ratio or in exchange of TCA cycle intermediates and amino acids with the extracellular medium.

Replicative senescence in HMECs is accompanied by significant alterations in nucleotide and nucleoside pool sizes

Next, we quantified the intracellular metabolite pool sizes in both proliferating and senescent HMECs. In five independent experiments, we measured 111 metabolites in at least two independent experiments (Table S2). Of the measured metabolites, 11 were significantly increased and 31 were significantly decreased in senescent cells (false discovery rate–corrected p value < 0.01). Notably, we did not observe significant change in the AMP/ATP ratio of senescent HMECs (Fig. S2*C*), in contrast to previous findings in senescent human fibroblasts (14, 36). Visualization of these data on a volcano plot revealed that several deoxyribonucleoside di- and triphosphates (dNDPs and dNTPs), including dCDP, dTDP, dADP, dATP, and dUTP, were significantly down-regulated in senescent cells (Fig. 2, *B* and *C*). Conversely, intracellular levels of guanine and uridine were significantly up-regulated. Increased intracellular levels of uridine were accompanied by increased secretion of uridine and the corresponding nucleobase uracil (Fig. 2*D*). Visualization of the $\log_2$ -fold changes in intracellular pool size on a metabolic pathway map also revealed decreased metabolite pool sizes for most of glycolysis, the TCA cycle, the pentose

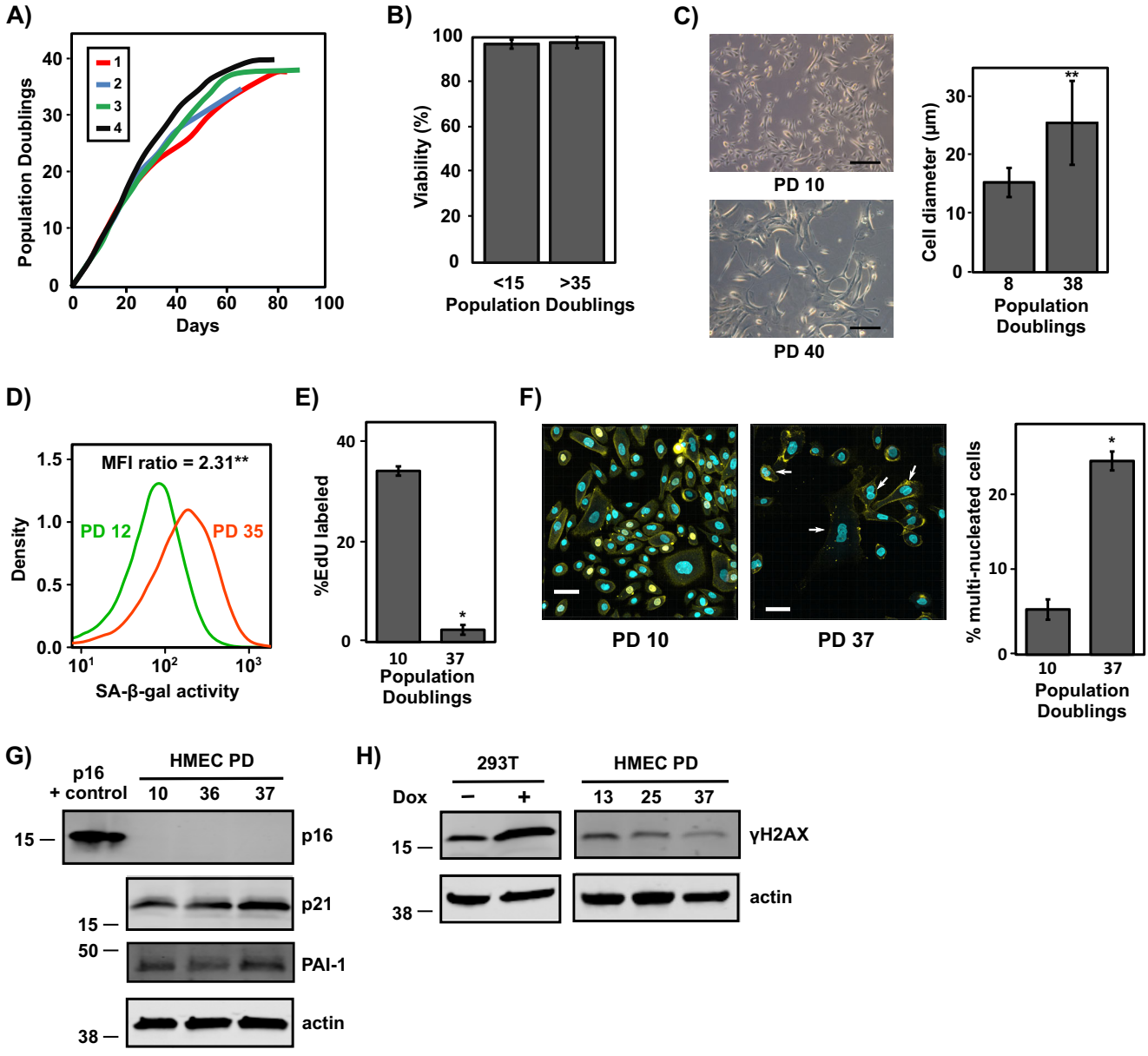

Figure 1. Establishment of an HMEC model of senescence. *A*, HMECs ceased proliferation at 35–40 population doublings. HMECs were cultured in M87A medium with medium replacement every 2 days (every day after 50% confluence) and passaged at 80–90% confluence (21). Four independent cultures are shown. *B*, HMEC viability was unaffected by senescence arrest. Viability of proliferating (<15 population doublings) and senescent (>35 population doublings) cells is shown. HMEC viability was measured by trypan blue staining. *C*, HMECs acquired enlarged, flattened, and irregular morphology at PD 40. Phase-contrast images and cell sizes are represented at PD 10 and 40. *Scale bar*, 100 μm. **, $p < 2 \times 10^{-16}$ by Mann–Whitney *U* test. *D*, HMECs showed increased activity of SA-β-gal at PD 35 measured by fluorescence signal of C_{12}FDG. SA-β-gal measurements are shown at PD 10 and 35. SA-β-gal activity was calculated as follows: mean of samples labeled with C_{12}FDG − mean of samples without C_{12}FDG. **, *p* value less than 0.0001 by Student's *t* test. *E*, measurement of DNA synthesis by EdU incorporation showed decreased DNA synthesis in senescent cells. **, $p < 0.001$ by Student's *t* test. *F*, immunofluorescence imaging of proliferating and senescent HMECs using Hoechst and membrane dye. HMECs at PD 37 showed an increased number of multinucleated cells (denoted by *arrows*). *Scale bar*, 50 μm. *, $p < 0.002$ by Student's *t* test. *G*, immunoblot for p16, p21, PAI-1, and actin with lysates from proliferating and senescent HMECs. Recombinant human p16 protein (40 ng) was used as a positive control in the p16 Western blotting. *H*, immunoblot for γ-H2AX and actin with lysates from proliferating and senescent HMECs. A lysate from the 293T cell line treated with the DNA-damaging agent doxorubicin (*Dox*; 1 μM for 24 h) or control was used as a positive control. Actin was used as an equal loading control. *Error bars*, S.D.

phosphate pathway, and nucleotide synthesis metabolites (Fig. 2*E*). Metabolite set enrichment set analysis demonstrated that nucleoside mono-/di-/triphosphates were the most significantly down-regulated metabolic pathway in senescent cells (Fig. S2*D*). Taken together, these data suggest that replicative senescence in HMECs induces dramatic changes in global metabolism with a particularly strong decrease in nucleotide metabolic pool sizes.

Glucose-derived carbon fuels nucleotide synthesis in proliferating but not senescent HMECs

Because changes in metabolite pool size do not always accurately reflect changes in metabolic flux (37), we next analyzed metabolic flux in proliferating and senescent HMECs by stable isotope labeling. We cultured proliferating and senescent HMECs with [U-^{13}C]glucose followed by LC-MS metabolomics. To gain a

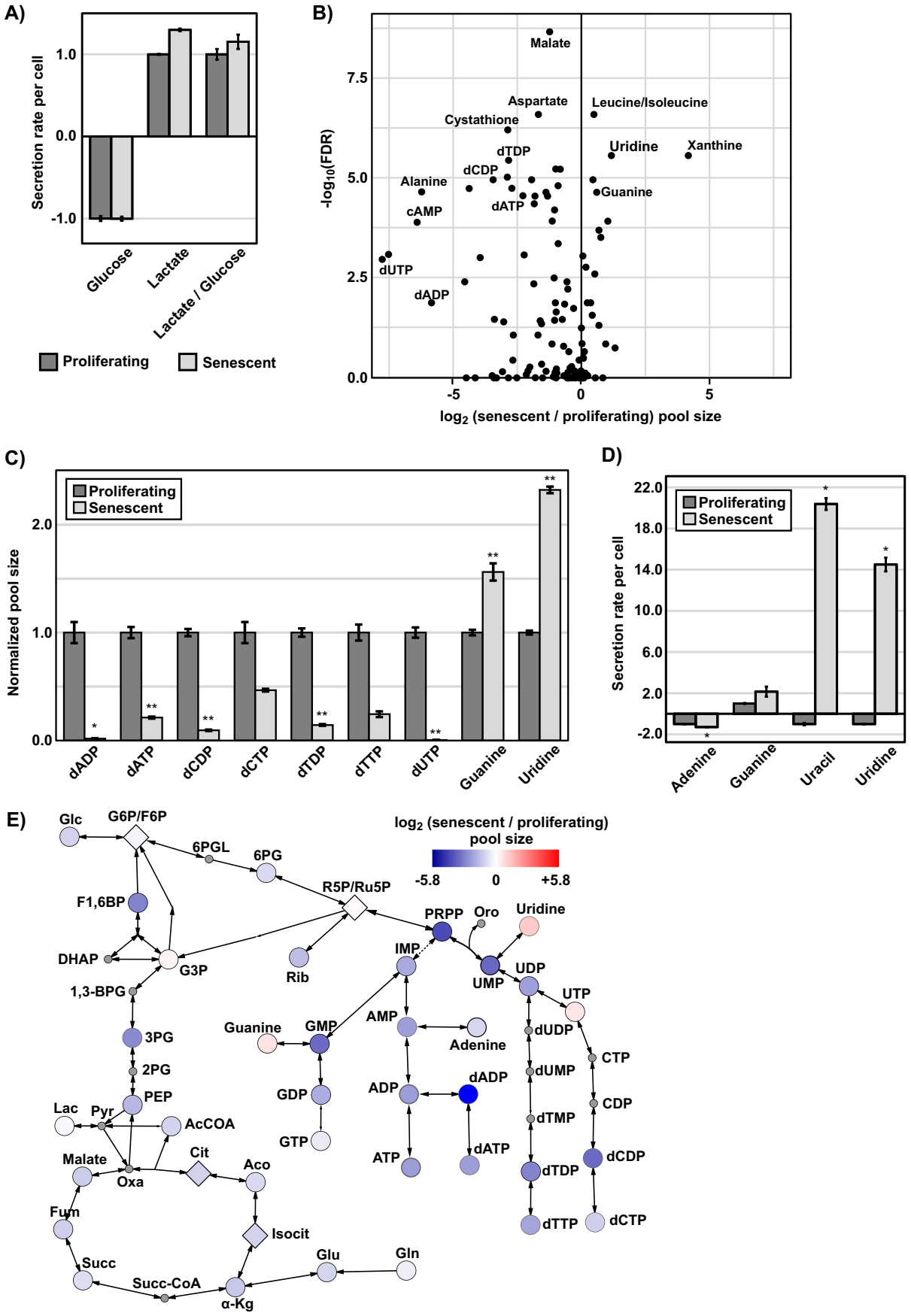
A)
Secretion rate per cell
1.0
0.0
-1.0
Glucose
Lactate
Lactate / Glucose
Proliferating
Senescent
B)
Malate
Aspartate
Cystathione
Leucine/Isoleucine
Uridine
Xanthine
dTDP
dCDP
Alanine
Guanine
dATP
cAMP
dUTP
dADP
-log10(FDR)
7.5
5.0
2.5
0.0
-5
0
5
log2 (senescent / proliferating) pool size
C)
Proliferating
Senescent
Normalized pool size
2.0
1.0
0.0
dADP
dATP
dCDP
dCTP
dTDP
dTTP
dUTP
Guanine
Uridine
D)
Proliferating
Senescent
Secretion rate per cell
22.0
18.0
14.0
10.0
6.0
2.0
-2.0
Adenine
Guanine
Uracil
Uridine
E)
log2 (senescent / proliferating) pool size
-5.8
0
+5.8
Glc
G6P/F6P
6PGL
6PG
R5P/Ru5P
F1,6BP
PRPP
Oro
Uridine
DHAP
G3P
Rib
IMP
UMP
UDP
UTP
1,3-BPG
Guanine
GMP
AMP
Adenine
dUDP
3PG
CTP
2PG
dUMP
CDP
PEP
GDP
ADP
dADP
Lac
Pyr
AcCOA
dTMP
GTP
ATP
dATP
Malate
Cit
Aco
dCDP
Oxa
dTDP
Fum
Isocit
dTTP
dCTP
Glu
Gln
Succ
Succ-CoA
α-Kg

global picture of the contribution of glucose-derived carbon to intermediary metabolites, we calculated glucose fractional contribution for each metabolite (38) (Table S3). Plotting the glucose fractional contribution on a volcano plot revealed that metabolites from the pyrimidine synthesis, including UMP, UDP, UTP, dCDP, dCTP, dTDP, and dTTP, showed significantly decreased incorporation of glucose-derived carbon (Fig. 3, *A* and *B*). Notably, whereas phosphoribosyl pyrophosphate (PRPP), one of the precursors for pyrimidine synthesis, demonstrated only a small change in glucose-derived carbon incorporation, UMP and the downstream products of pyrimidine synthesis (*e.g.* dCDP) exhibited almost complete loss of glucose-derived carbon incorporation (Fig. 3, *B* and *C*). Visualization of the [U-^{13}C]glucose fractional incorporation on a metabolic pathway map confirmed that the pyrimidine synthesis pathway demonstrated the largest decrease in glucose fractional incorporation (Fig. 3*D*). In contrast, metabolites from the TCA cycle showed little to no change in [U-^{13}C]glucose fractional incorporation or isotopomer distributions (Fig. S3).

We next used [1,2-^{13}C]glucose to investigate possible alterations in the ratio of glucose that enters the pentose phosphate pathway *versus* glycolysis (39). However, we observed no significant difference in the percentages of M1 and M2 lactate when comparing proliferating and senescent cells (Fig. S4*A*). There was, however, a significant decrease of ^{13}C incorporation into UMP and downstream pyrimidines, consistent with our observation using U-^{13}C–labeled glucose (Fig. S4 (*B* and *C*) and Table S4). Next, we analyzed proliferating and senescent HMECs labeled with [U-^{13}C]glutamine to test for changes in TCA cycle flux. We observed a decreased ratio of reductive to oxidative flux in the TCA cycle for senescent HMECs; however, the -fold change was small (Fig. S4*D*). Visualization of the [U-^{13}C]glutamine fractional contribution to metabolites revealed significant changes in the contribution of glutamine-derived carbon to pyrimidine synthesis (Fig. S4 (*E* and *F*) and Table S5). Taken together, these data suggest that senescent cells strongly downregulate the flux of carbon into pyrimidine synthesis while leaving glycolysis and the TCA cycle unaffected.

We next queried published gene expression data to ask whether inhibition of nucleotide synthesis is broadly reflected at the transcriptional level in senescent cells. We analyzed (i) microarray data from HMECs in replicative senescence (*i.e.* stasis) (22) and (ii) RNA-Seq data from IMR90 fibroblasts induced to senesce by ionizing radiation (2). Gene set expression analysis (GSEA) (40) across all KEGG metabolic pathways ($n = 78$) (41) demonstrated a robust suppression of both pyrimidine metabolism (hsa00240) and purine (hsa00230) pathways in senescent cells (Fig. S5 (*A* and *B*) and Table S6). In both data sets, expression of RRM2, which catalyzes the biosynthesis of deoxyribonucleotides from ribonucleotides, was strongly decreased in senescent cells (not shown). Consistent with these data, Western blotting in our HMECs demonstrated down-regulation of RRM2 in senescent cells (Fig. 3*E* and Fig. S5*C*). Taken together, these data suggest that senescent HMECs exhibit reduced nucleotide synthesis.

HMEC immortalization with telomerase restores nucleotide pools and fluxes

Because transduction of HMECs with exogenous hTERT can immortalize pre-stasis HMECs (42), we next tested the effects of hTERT-mediated immortalization on the metabolic profiles of HMECs. We expressed either hTERT or a firefly luciferase control in proliferating HMECs (PD 13). hTERT-expressing HMECs continued to grow logarithmically in culture, whereas HMECs expressing luciferase ceased to proliferate at PD ~33 (Fig. 4*A*). 60 days after transduction with luciferase and hTERT (PD 35 and 85 for luciferase and hTERT, respectively), we observed cuboidal cell morphology in hTERT-expressing cells, similar to proliferating, nonimmortalized HMECs (Fig. 4*B*). In contrast, luciferase-expressing cells acquired a senescent morphology and exhibited increased SA-β-gal activity (Fig. 4, *B* and *C*). Next, we confirmed that senescent luciferase-expressing HMECs exhibited a lack of DNA synthesis (Fig. 4*D*) and increased expression of the senescence markers p21 and PAI-1 (Fig. 4*E*). Taken together, these data demonstrate that hTERT expression efficiently immortalized HMECs.

We then profiled luciferase- and hTERT-expressing HMECs using LC-MS metabolomics. Consistent with unmodified HMECs, medium footprint analysis revealed that glucose consumption and lactate secretion rates were not significantly different in proliferating, hTERT-expressing and senescent, luciferase-expressing cells (Fig. S6 and Table S7). Secretion of guanine and uridine was increased in senescent, luciferase-expressing HMECs. We next examined intracellular metabolite pool sizes in luciferase- and hTERT-expressing cells at days ~15 and ~60 following viral transduction and drug selection. At day ~15, both luciferase- and hTERT-expressing cells were proliferating, whereas at day ~60, luciferase- but not hTERT-expressing cells were senescent. Metabolomic profiling demonstrated that hTERT-expressing cells experienced no significant changes in dNDP and dNTP pool sizes between days ~15 and ~60 (Fig. 4*F* and Table S8). In contrast, luciferase-expressing cells exhibited significantly decreased dNDP and dNTP metabolite pool sizes, closely mirroring observations in untransduced proliferating and senescent HMECs.

Figure 2. Replicative senescence in HMECs is accompanied by significant alterations in metabolite pool sizes. *A*, glucose consumption, lactate secretion, and ratio of glucose consumption to lactate secretion are unchanged in senescent HMECs. Metabolite extracts from blank and conditioned media were analyzed by LC-MS. Secretion or uptake is calculated as follows: conditioned medium − blank medium, normalized to integrated cell number. Secreted metabolites have positive values, and consumed metabolites have negative values. *B*, *volcano plot* of intracellular pool sizes for all measured metabolites. Data represent average weighted $\log_2$ -fold change (senescent/proliferating) and FDR-corrected Fisher's combined *p* value from five independent experiments. Depicted metabolites were measured in at least two independent experiments. *C*, depletion of dNDPs and dNTPs and accumulation of nucleobases and nucleosides in senescent HMECs (same data as in *B* for selected dNDPs, dNTPs, guanine, and uridine). * and **, FDR-corrected Student's *t* test *p* values less than 0.02 and 0.002, respectively. *D*, extracellular secretion and consumption measured by LC-MS as in *A* for the nucleobases adenine, guanine, and uracil and the nucleoside uridine. Secreted metabolites have positive values, and consumed metabolites have negative values. *, FDR-corrected Student's *t* test $p < 0.001$. *E*, metabolic pathway map depicting the $\log_2$ -fold change (senescent/proliferating) intracellular pool sizes of metabolites in glycolysis, pentose phosphate pathway, nucleotide synthesis, and TCA cycle using the indicated *color scale*. Metabolites that were not measured are shown as *small circles* with *gray color*. Isomers that were not resolved with LC-MS are shown as *diamonds*. *Error bars*, S.D.

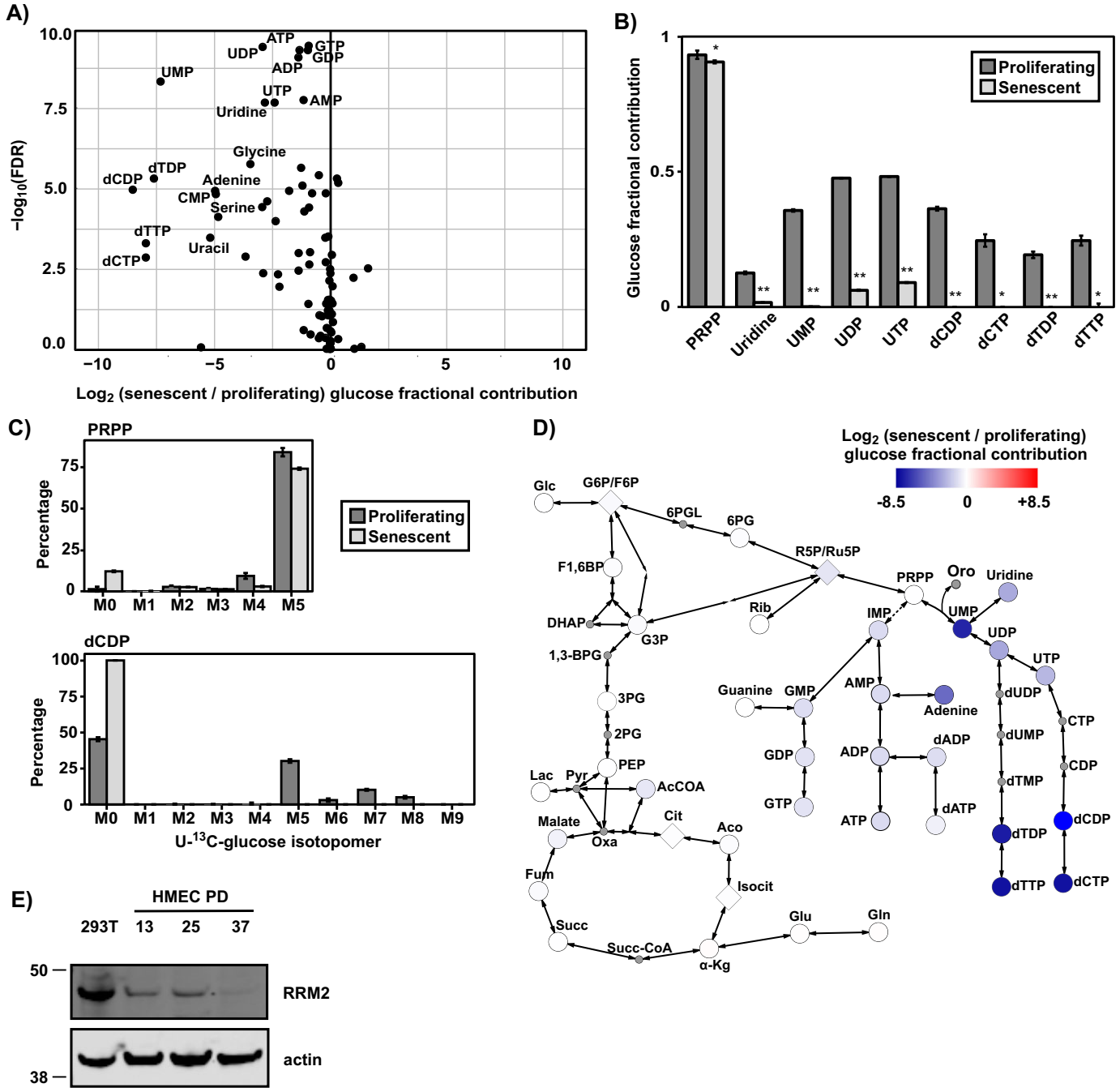

Figure 3. Glucose-derived carbon fuels nucleotide synthesis in young but not senescent HMECs. *A*, purine and pyrimidine metabolites show significantly reduced [U-^{13}C]glucose carbon labeling in senescent HMECs. The *volcano plot* represents the average $\log_2$ -fold change (senescent/proliferating) for fractional contribution (38) of U-^{13}C–labeled glucose and FDR-corrected Fisher's combined *p* value from two independent experiments. *B*, glucose flux into nucleotide synthesis pathways is globally reduced in senescent HMECs. Shown is the fractional contribution of U-^{13}C-labeled glucose for selected pyrimidines. * and **, FDR-corrected Student's *t* test *p* values less than 0.01 and 0.0001, respectively. *C*, [U-^{13}C]glucose isotopomer distributions for dCDP but not PRPP are significantly different in senescent HMECs. *D*, metabolic pathway map depicting the average $\log_2$ -fold change of fractional contribution from [U-^{13}C]glucose in senescent/proliferating HMECs on the indicated *color scale* for metabolites in glycolysis, pentose phosphate pathway, nucleotide synthesis, and the TCA cycle. Metabolites that were not measured are shown as *small circles* with *gray color*. Metabolites with isomers that were not resolved on LC-MS are shown as *diamonds*. *E*, immunoblot for RRM2 and actin with lysates from proliferating and senescent HMECs. A protein lysate from the 293T cell line was used as a positive control, and actin was used as an equal loading control. The RRM2 antibody was obtained from GeneTex. *Error bars*, S.D.

Next, we used U-^{13}C–labeled glucose to assess the fractional contribution of glucose to the metabolism of HMECs expressing hTERT and luciferase. This analysis revealed that [U-^{13}C]glucose fractional incorporation in hTERT-expressing cells was unchanged between days ~15 and ~60 for pyrimidines and purines, including UMP, UDP, UTP, dADP, dATP, dTDP, and dCDP (Fig. 4*G* and Fig. S7 and Table S9). In contrast, luciferase-expressing HMECs exhibited significantly reduced fractional incorporation of [U-^{13}C]glucose into these pyrimidines and purines, similar to observations in untransduced proliferating and senescent HMECs.

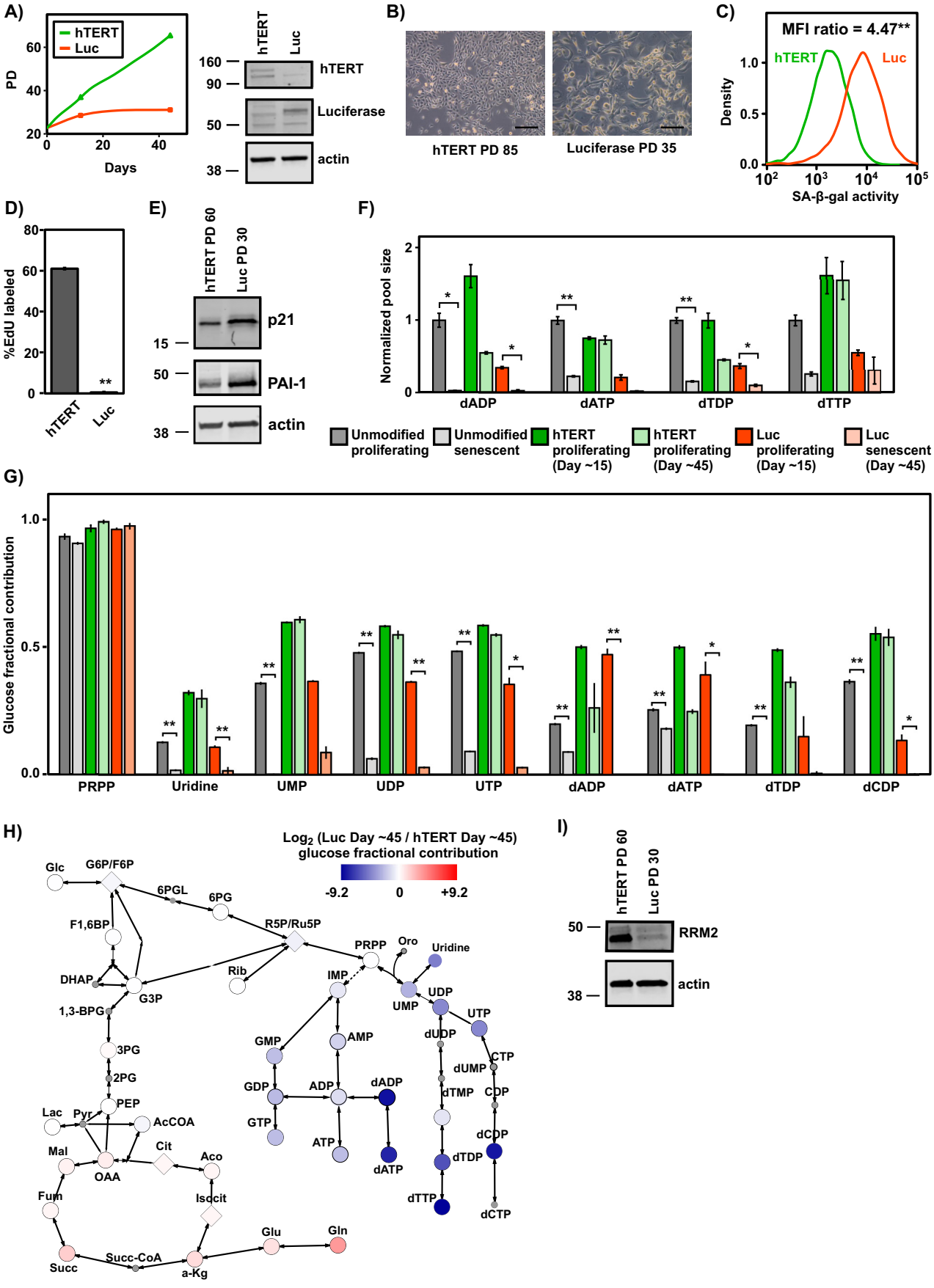
A)
hTERT
Luc
PD
Days
hTERT
Luc
160
90
50
38
hTERT
Luciferase
actin
B)
hTERT PD 85
Luciferase PD 35
C)
MFI ratio = 4.47**
hTERT
Luc
Density
SA-β-gal activity
D)
%EdU labeled
hTERT
Luc
E)
hTERT PD 60
Luc PD 30
p21
PAI-1
actin
F)
Normalized pool size
dADP
dATP
dTDP
dTTP
Unmodified proliferating
Unmodified senescent
hTERT proliferating (Day ~15)
hTERT proliferating (Day ~45)
Luc proliferating (Day ~15)
Luc senescent (Day ~45)
G)
Glucose fractional contribution
PRPP
Uridine
UMP
UDP
UTP
dADP
dATP
dTDP
dCDP
H)
Log2 (Luc Day ~45 / hTERT Day ~45) glucose fractional contribution
-9.2
0
+9.2
Glc
G6P/F6P
6PGL
6PG
F1,6BP
R5P/Ru5P
PRPP
Oro
Uridine
DHAP
Rib
IMP
G3P
UDP
UMP
UTP
1,3-BPG
GMP
AMP
dUDP
CTP
3PG
dUMP
2PG
GDP
ADP
dADP
dTMP
CDP
PEP
Lac
Pyr
AcCOA
GTP
ATP
dCDP
Cit
Mal
Aco
dTDP
dATP
OAA
dTTP
Fum
Isocit
dCTP
Glu
Gln
Succ-CoA
Succ
a-Kg
I)
hTERT PD 60
Luc PD 30
RRM2
actin

Visualization of the glucose fractional contribution on a metabolic pathway map confirmed a global inhibition of carbon flux to nucleotides downstream of PRPP (Fig. 4*H*). In addition, metabolite set enrichment set analysis confirmed that nucleoside mono-/di-/triphosphates exhibited significantly decreased [U-^{13}C]glucose-derived label in senescent, luciferase-expressing HMECs (Fig. S8). Notably, hTERT also induced moderate down-regulation of glucose-derived carbon to TCA cycle metabolites, a difference that was not observed comparing unmodified proliferating and senescent HMECs. Finally, we measured protein expression of RRM2 using Western blotting and observed significant decrease in high-PD senescent luciferase-expressing HMECs (Fig. 4*I*). Taken together, these results demonstrate that hTERT immortalization maintains nucleotide pools and fluxes in HMECs.

Inhibiting ribonucleotide reductase induces senescence

Based on the metabolomic profile of senescent and proliferating HMECs, we hypothesized that reduced nucleotide synthesis plays a causative role in induction of senescence. To test this hypothesis, we first treated proliferating HMECs with triapine, an inhibitor of RRM2 (43). Indeed, treatment of proliferating HMECs (PD 10) with triapine effectively blocked cell proliferation (Fig. 5*A*). Following triapine treatment, cells acquired a typical senescent morphology and were significantly increased in size (Fig. 5*B*). Additionally, triapine-treated HMECs exhibited increased SA-β-gal activity (Fig. 5*C*), reduced DNA synthesis (Fig. 5*D*), and increased expression of p21 and PAI-1 (Fig. 5*E* and Fig. S9*A*). To confirm the role of RRM2 in senescence, we next used CRISPRi-mediated knockdown of RRM2 expression (CRISPR-dCas9-KRAB) (44). Expression of a sgRNA against RRM2 but not a nontargeting sgRNA control efficiently knocked down RRM2 expression and inhibited cell growth in proliferating HMECs (Fig. 5*F*). We then confirmed that RRM2 knockdown increased SA-β-gal activity (Fig. 5*G*), reduced DNA synthesis (Fig. 5*H*), and increased expression of p21 and PAI-1 (Fig. 5*I* and Fig. S9*B*). Taken together, these data demonstrate that inhibition of RRM2 is sufficient to induce senescence in primary HMECs.

Next, we tested whether inhibition of RRM2 could induce senescence in the immortalized but nontransformed mammary epithelial cell line MCF10A. Indeed, triapine treatment slowed cell growth, induced SA-β-gal activity, reduced DNA synthesis, and increased expression of p21 and PAI-1 (Fig. S9, *C–G*). Together with data from primary HMECs, these data demonstrate that inhibition of RRM2 activity can induce senescence in immortalized mammary epithelial cells.

To investigate metabolomic alterations upon triapine-induced senescence, we again performed untargeted LC-MS metabolomics. HMECs treated with triapine exhibited depleted dNDP and dNTP pool sizes and increased intracellular levels of the nucleoside uridine (Fig. 5*J*). In contrast, we observed no significant change in the intracellular pool sizes of glucose, ribose 5-phosphate, and PRPP (Fig. 5*J* and Table S10). Tracing U-^{13}C–labeled glucose in triapine-treated HMECs highlighted the down-regulation of glucose flux into nucleotide biosynthesis (Fig. 5*K*). Examination of the U-^{13}C–labeled glucose incorporation levels in triapine-treated cells showed that fractional contribution of glucose to PRPP was not significantly changed, similar to replicative senescence (Fig. 5 (*K* and *L*) and Table S11). However, there was a significant inhibition of glucose flux into pyrimidines in triapine-induced senescent HMECs (Fig. 5, *K* and *L*). In contrast, glucose flux into the TCA cycle did not significantly change upon triapine treatment (Fig. 5*L*). Metabolite set enrichment set analysis demonstrated that nucleoside and deoxynucleoside mono-/di-/triphosphates were the most significantly decreased metabolic pathways in triapine-induced senescent cells (Fig. S10). Taken together, these results indicate that inhibition of nucleotide synthesis is sufficient to trigger senescence in nonimmortalized HMECs.

Integrative analysis of glucose contribution to metabolites in proliferating and senescent HMECs

To identify the most consistent alterations in senescent cells across our metabolomic experiments, we conducted unsupervised hierarchical clustering of the glucose fractional contribution to each metabolite across experiments. Proliferating HMEC cultures (low PD, hTERT expression, and DMSO treatment) and senescent HMEC cultures (high PD, luciferase expression, and triapine treatment) were separated into two well-defined clusters (Fig. 6). In addition, nucleotides were tightly clustered together to reveal decreased levels of glucose-

Figure 4. hTERT immortalization restores nucleotide pools and fluxes. *A*, expression of hTERT in proliferating HMECs prevented occurrence of senescence growth arrest. Shown is a representative growth curve demonstrating that hTERT-expressing HMECs continued to grow logarithmically in culture, whereas HMECs expressing luciferase ceased to proliferate at PD ~33. *Filled triangles* and *squares* indicate the PD at which cells were extracted for metabolomics. The *x axis* represents days since completion of drug selection. hTERT and luciferase expression were confirmed by Western blotting. Actin was used as an equal loading control. *B*, phase-contrast images of luciferase- and hTERT-expressing HMECs at PD 35 and 85, respectively. Luciferase-expressing HMECs acquired enlarged, flattened, and irregular morphology typical of senescent cells. hTERT-expressing HMECs maintained their epithelial cell morphology. *Scale bar*, 100 μm. *C*, luciferase-expressing HMECs showed increased activity of SA-β-gal measured by fluorescence signal of C_{12}FDG at SA-β-gal measurements are shown at day ~60 following drug selection. SA-β-gal activity was calculated as follows: mean of samples labeled with C_{12}FDG − mean of samples without C_{12}FDG. **, $p < 0.0001$ by Student's *t* test. *D*, measurement of DNA synthesis by EdU incorporation showed decreased DNA synthesis in senescent, luciferase-expressing cells at day ~45 following drug selection. **, $p < 0.00004$ by Student's *t* test. *E*, immunoblot for p21, PAI-1, and actin with lysates from luciferase- and hTERT-expressing HMECs at day ~45 following drug selection. *F*, hTERT-expressing HMECs maintain purine and pyrimidine pools. Luciferase- and hTERT-expressing cells were profiled by LC-MS metabolomics at days ~15 and ~45 following drug selection. Luciferase-expressing cells were senescent at day ~45, but all other samples were still proliferating. Data from proliferating (PD 9) and senescent primary HMECs (PD 37) is shown for comparison. * and **, $p < 0.04$ and 0.008, respectively. *G*, hTERT-expressing HMECs maintain glucose flux to purines and pyrimidines as measured by fractional contribution of U-^{13}C–labeled glucose for selected purines and pyrimidines, as well as the nucleotide synthesis precursor PRPP. The number of days following drug selection for hTERT- and luciferase-expressing HMECs was the same as in *F*. Data from proliferating and senescent primary HMECs are shown for comparison. * and **, *p* value less than 0.04 and 0.002, respectively. *H*, metabolic pathway map depicting the average $\log_2$ -fold change of [U-^{13}C]glucose fractional contribution for senescent, luciferase-expressing (day ~45) compared with proliferating, hTERT-expressing cells (day ~45) on the indicated *color scale* for metabolites in glycolysis, pentose phosphate pathway, nucleotide synthesis, and the TCA cycle. Metabolites that were not measured are shown as *small circles* with *gray color*. Isomers that were not resolved with LC-MS are shown as *diamonds*. *I*, immunoblot for RRM2 and actin with lysates from senescent, luciferase-expressing and proliferating, hTERT-expressing HMECs. *Error bars*, S.D.

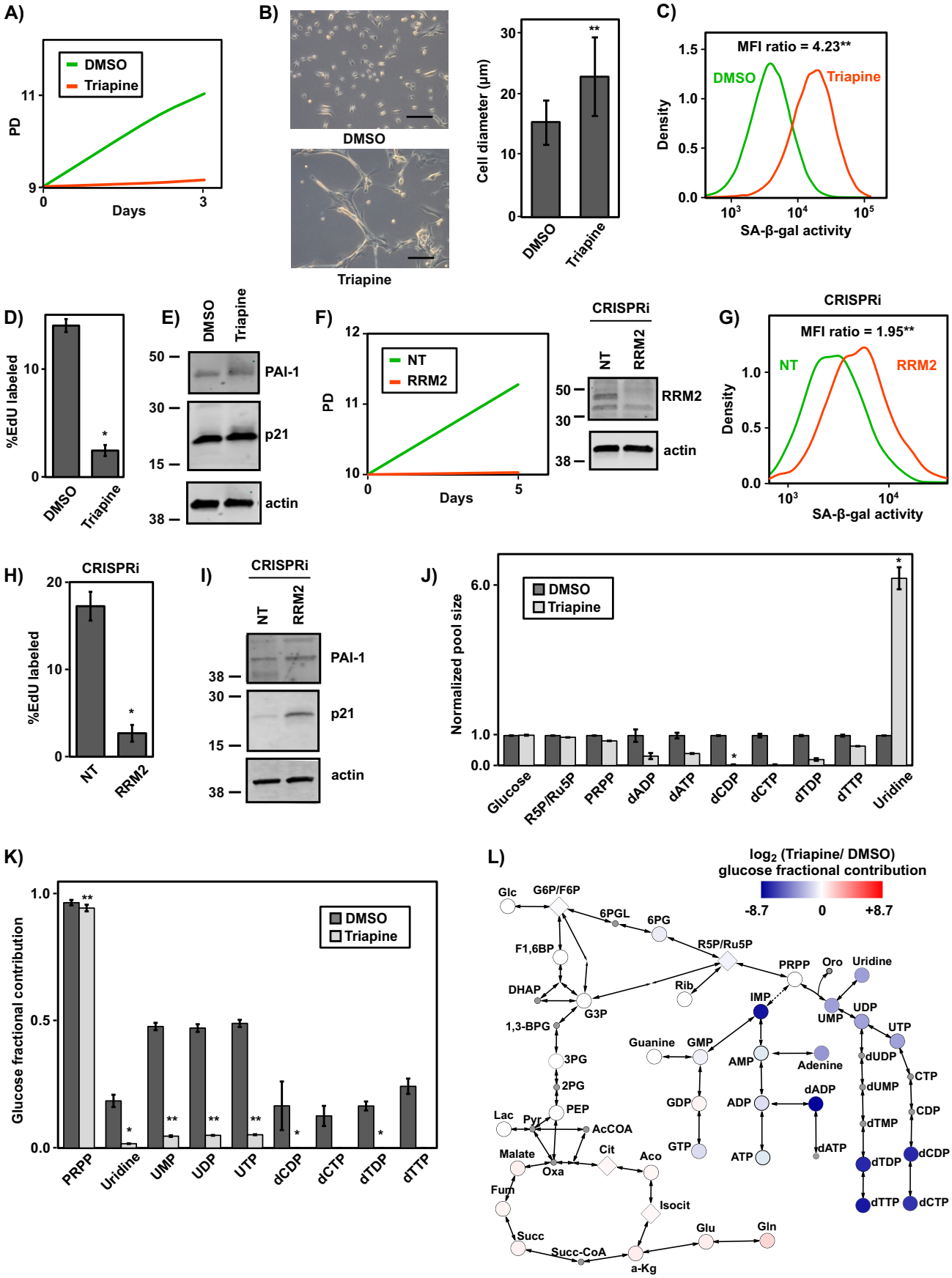
A)
DMSO
Triapine
PD
Days
B)
DMSO
Triapine
Cell diameter (μm)
C)
MFI ratio = 4.23**
DMSO
Triapine
Density
SA-β-gal activity
D)
%EdU labeled
E)
PAI-1
p21
actin
F)
NT
RRM2
PD
Days
CRISPRi
G)
MFI ratio = 1.95**
H)
I)
J)
Normalized pool size
Glucose
R5P/Ru5P
PRPP
dADP
dATP
dCDP
dCTP
dTDP
dTTP
Uridine
K)
Glucose fractional contribution
L)
log2 (Triapine/ DMSO)
glucose fractional contribution
-8.7
0
+8.7
Glc
G6P/F6P
6PGL
6PG
F1,6BP
R5P/Ru5P
PRPP
Oro
Uridine
DHAP
Rib
IMP
UDP
UMP
UTP
G3P
1,3-BPG
Guanine
GMP
AMP
Adenine
dUDP
3PG
dADP
CTP
2PG
GDP
ADP
dUMP
CDP
Lac
Pyr
PEP
AcCOA
dTMP
GTP
ATP
dATP
Malate
Cit
Aco
Oxa
dTDP
dCDP
Fum
Isocit
dTTP
dCTP
Glu
Gln
Succ
Succ-CoA
a-Kg

derived carbon incorporation in senescent cells (*red cluster*). This *heat map* also highlighted the moderate down-regulation of glucose contribution to TCA cycle metabolites in hTERT-expressing HMECs (*blue cluster*). Taken together, this confirms that inhibited nucleotide synthesis is a hallmark of senescent HMECs.

Discussion

Cellular senescence is a state of irreversible cell cycle arrest that contributes to degenerative and hyperplastic phenotypes in aging and cancer. Although senescent cells are withdrawn from the cell cycle, they remain highly metabolically active (11). Here, we show that inhibition of nucleotide synthesis regulates replicative senescence in primary HMECs. The inhibition of nucleotide synthesis in senescent HMECs was reflected both in reduced pool sizes (Fig. 2*E*) and in reduced metabolic flux into nucleotide synthesis (Fig. 3*D* and Fig. S4). In contrast, fluxes from glucose and glutamine into glycolysis, the pentose phosphate pathway, and the TCA cycle were not significantly changed. Importantly, treatment of proliferating HMECs with an inhibitor of RRM2, a key enzyme in dNTP synthesis, demonstrated that inhibition of nucleotide synthesis was sufficient to induce senescence and recapitulate the metabolomic signature of HMEC replicative senescence. Taken together, these findings demonstrate the crucial role of nucleotide synthesis in cellular senescence of a primary epithelial cell type, a finding with implications for both aging and tumor development.

The study of metabolism during replicative senescence has relied heavily on fibroblasts, a mesenchymal cell type. These studies have demonstrated that human fibroblasts gradually exhibit a more glycolytic metabolism as they become senescent (12–14). Similarly, senescence induced by oncogene activation also leads to increased glycolysis (8, 16). Here, using a primary epithelial cell type (HMEC), we did not observe significant alterations in either glucose uptake or lactate secretion in senescent HMECs (Fig. 2*A*). Additionally, the fractional contribution of glucose and glutamine to glycolysis and the TCA cycle was unchanged in senescent HMECs. In contrast to senescent fibroblasts (14), HMEC senescence was also not accompanied by an energy crisis (Fig. S2*C*). Taken together, these results suggest that epithelial and fibroblast cells exhibit distinct metabolic alterations during senescence. These metabolic differences may reflect the fact that senescent epithelial and fibroblast cells exhibit distinct transcriptional profiles (22).

Although replicative senescence in our HMEC system does not involve oncogene activation, the inhibition of nucleotide synthesis we observed resembles the metabolic alterations found in oncogene-induced senescence. Notably, in fibroblasts, oncogenic RAS induces senescence by suppressing nucleotide metabolism, leading to the depletion of dNTP pools (6, 9). This depletion of dNTP pools is mediated by RAS-induced repression of RRM2 mRNA and protein levels. Similarly, senescent HMECs showed a significant down-regulation of RRM2 protein expression (Fig. 3*E* and Fig. S5*C*). Notably, in HMECs, chemical inhibition of RRM2 was sufficient to induce senescence and recapitulated the metabolomic signature of senescent HMECs (Figs. 5 and 6). Together, our findings extend the relevance of nucleotide metabolism in senescence to a non-transformed, primary cell type in the absence of oncogene activation.

In the current study, we observed depletion of dNTPs in the absence of γ-H2AX induction, suggesting that senescent HMECs do not experience DNA double-strand breaks during the time course of our experiments (Fig. 1*E*). However, because the maintenance of sufficient and balanced dNTP pools is essential for maintaining genomic integrity (45, 46), the inability to synthesize dNTPs may eventually lead to replication stress, genomic instability, and mutagenesis (47, 48). Indeed, genomic instability in the early stages of tumorigenesis induced by cyclin E oncogenes is coupled to insufficient nucleotide availability (49). In addition, we observed a significantly increased number of multinucleated cells in the senescent HMEC culture, which has previously been linked to genomic instability (50), telomere dysfunction (51), polyploidy (52), and tumor initiation (28). Additionally, the extent of senescence experienced by mouse embryonic fibroblasts during immortalization correlates with the amount of genomic instability in immortalized cell lines (34). Interestingly, in RAS-expressing fibroblasts, senescence-associated nucleotide deficiencies can be bypassed by inactivation of the serine/threonine kinase ATM, which is activated by DNA damage (53). However, because senescent HMECs in this study are not experiencing DNA double-strand breaks, they may more closely resemble hypoxic cells, which experience replication stress but not DNA damage (54). Similar to hypoxic cells, senescent cells up-regulate RRM2B (55), a subunit of the ribonucleotide reductase complex that may pre-

Figure 5. Inhibiting ribonucleotide reductase induces senescence. *A*, treating proliferating HMECs with the RRM2 inhibitor triapine inhibits cell growth. Cells at PD ~8 were treated with 2 μM triapine or DMSO for 72 h. *B*, phase-contrast images and cell sizes of HMECs treated with triapine or DMSO. HMECs acquire enlarged, flattened, and irregular morphology typical of senescent cells within 3 days of treatment with triapine. *Scale bar*, 100 μm. **, $p < 2 \times 10^{-16}$ by Mann–Whitney *U* test. *C*, triapine-treated HMECs showed increased activity of SA-β-gal measured by fluorescence signal of C_{12}FDG. SA-β-gal activity was calculated as follows: mean of samples labeled with C_{12}FDG − mean of samples without C_{12}FDG). **, $p < 0.0001$ by Student's *t* test. *D*, measurement of DNA synthesis by EdU incorporation showed decreased DNA synthesis in triapine-treated cells. *, $p < 0.003$ by Student's *t* test. *E*, Western blotting of p21, PAI-1, and actin for triapine-treated cells. *F*, genetic knockdown of RRM2 expression inhibits HMEC growth. Cells at PD ~10 were infected with sgRNA against RRM2 or nontargeting control. Western blotting of RRM2 and actin for HMECs infected with sgRNA against RRM2 or nontargeting control. *G*, knockdown of RRM2 expression induces SA-β-gal. SA-β-gal was measured by the fluorescence signal of C12FDG. SA-β-gal activity was calculated as follows: mean of samples labeled with C12FDG − mean of samples without C12FDG. **, $p < 0.0001$ by Student's *t* test. *H*, measurement of DNA synthesis by EdU incorporation showed decreased DNA synthesis in RRM2 knockdown cells. *, $p < 0.02$ by Student's *t* test. *I*, Western blotting of p21, PAI-1, and actin for HMECs infected with sgRNA against RRM2 or nontargeting control. *J*, triapine treatment results in depletion of dNDPs and dNTPs and induces uridine accumulation. *, $p < 0.003$ by Fisher's combined *t* test. *K*, fractional contribution of U-^{13}C–labeled glucose for selected pyrimidines. * and **, *p* values less than 0.03 and 0.0001 by Fisher's combined *t* test, respectively. *L*, metabolic pathway map depicting average $\log_2$ -fold change of [U-^{13}C]glucose fractional incorporation for triapine/DMSO on the indicated *color scale* for metabolites in glycolysis, pentose phosphate pathway, nucleotide synthesis, and the TCA cycle. Metabolites that were not measured are shown as *small circles* with *gray color*. Isomers that were not resolved with LC-MS are shown as *diamonds*. *Error bars*, S.D.

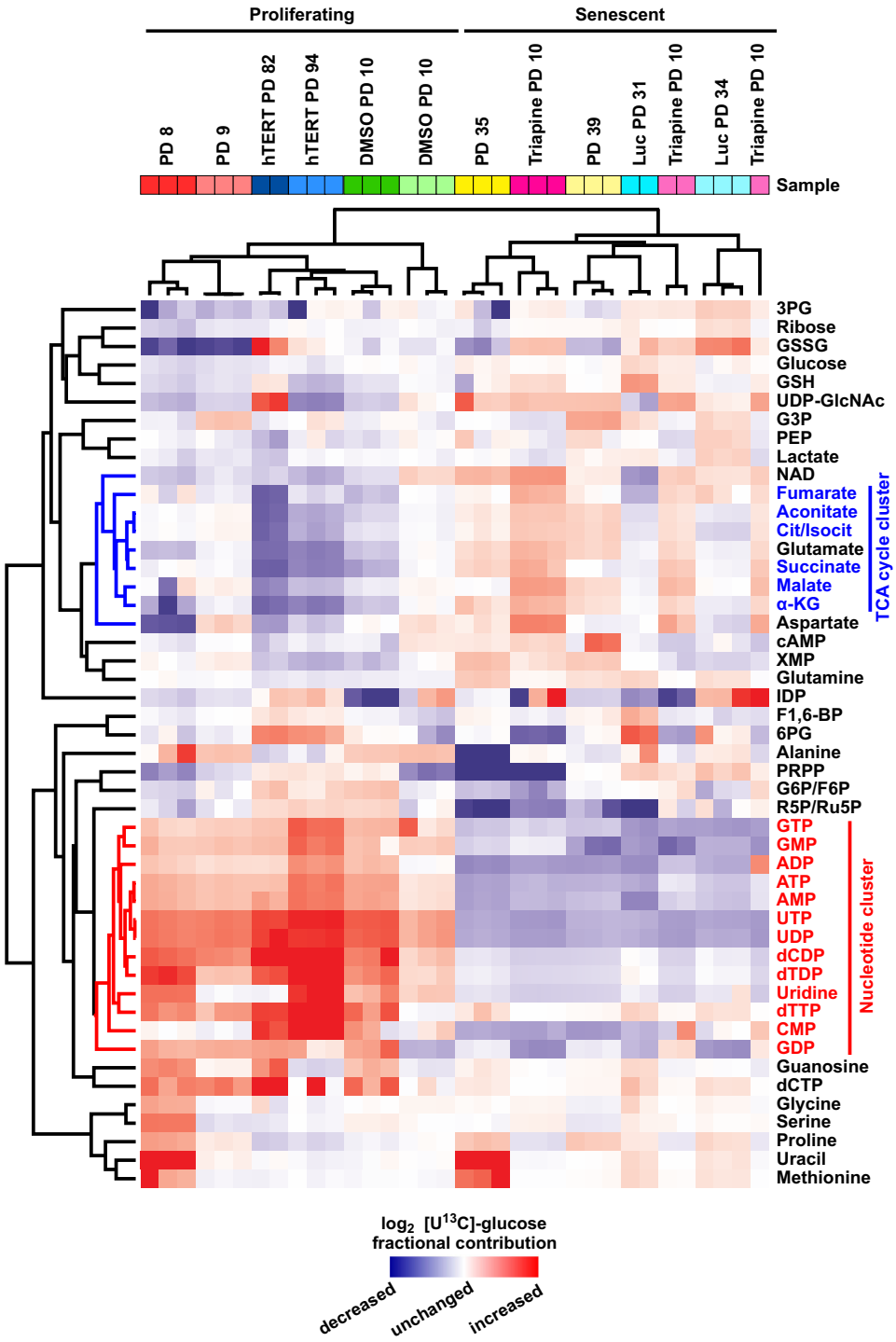

Figure 6. Integrative analysis of glucose contribution to metabolites in proliferating and senescent HMECs. Shown is a *heat map* comparing fractional contribution of glucose with commonly measured metabolites. *Columns* represent individual samples. *Red* indicates up-regulation, and *blue* indicates down-regulation. Nucleotides cluster together and are up-regulated in proliferating samples compared with senescent samples. *Error bars*, S.D.

serve the capacity for sufficient nucleotide synthesis during hypoxia to avoid DNA damage.

In senescent HMECs, we observed that the flux of glucose-derived carbon was more severely down-regulated in pyrimidine synthesis than in purine synthesis (Figs. 3*D*, 4*H*, and 5*L*). This difference between pyrimidine and purine synthesis was not reflected in metabolite pool sizes, highlighting the power of stable isotope tracing to reveal metabolic changes not apparent in metabolite pool sizes (37, 56). Pyrimidine synthesis can be specifically controlled through mTOR/S6K1-mediated phosphorylation of CAD (carbamoyl-phosphate synthetase 2, aspartate transcarbamylase, and dihydroorotase), the enzyme that catalyzes the first three steps of *de novo* pyrimidine synthesis (57). Additionally, loss of urea cycle enzymes, including carbamoyl phosphate synthetase-1 (CPS1), can lead to pyrimidine but not purine depletion (58). Although it is not yet

clear why pyrimidines are more affected than purines in senescent HMECs, this observation remains a subject of active investigation.

Taken together, our results indicate that suppression of nucleotide synthesis is a critical metabolomic alteration regulating senescence in primary HMECs. A more detailed understanding of altered metabolism as both a cause and a consequence of senescence will have important implications. In both aging (2) and cancer (59), therapeutic targeting of senescence has shown great promise. Similarly, therapeutics targeting the emerging metabolic differences between senescent and nonsenescent cells may prove useful tools for improving human health.

Experimental procedures

Cell culture

HMECs were purchased from Thermo Scientific and cultured in M87A medium (50% MM4 medium and 50% MCDB170 supplemented with 5 ng/ml epidermal growth factor, 300 ng/ml hydrocortisone, 7.5 μg/ml insulin, 35 μg/ml bovine pituitary extract, 2.5 μg/ml transferrin, 5 μM isoproterenol, 50 μM ethanolamine, 50 μM *o*-phosphoethanolamine, 0.25% FBS, 5 nM triiodothyronine, 0.5 nM estradiol, 0.5 ng/ml cholera toxin, 0.1 nM oxytocin, 1% antibiotic-antimycotic, no AlbuMax) in atmospheric oxygen. MCF10A cells were obtained from the American Tissue Culture Collection (ATCC) and cultured in Dulbecco's modified Eagle's medium/F-12 medium supplemented with 20 ng/ml epidermal growth factor, 500 ng/ml hydrocortisone, 100 μg/ml insulin, 100 ng/ml cholera toxin, 0.1 nM oxytocin, 5% horse serum, and 1× penicillin/streptomycin in atmospheric oxygen. Glucose and glutamine-free Dulbecco's modified Eagle's medium was purchased from Corning (90-113-PB), Ham's F-12 was purchased from US Biological (N8542-12), and MCD170 medium was purchased from Caisson Labs (MBL04). Glucose and glutamine were added to the media at the appropriate concentration for each medium type. Cells were lifted with TrypLE at 80–90% confluence and seeded at a density of $2.3 \times 10^3/cm^2$. Cell viability and diameter were measured with a trypan blue assay using a TC20 automated cell counter (Bio-Rad).

Genetic modification

Proliferating HMECs were infected at PD 14 with pLenti-PGK-hygro (Addgene 19066) encoding either hTERT or firefly luciferase. Following infection, cells were selected with 5 μg/ml hygromycin for 7 days. Following selection, cells were maintained in culture with 2 μg/ml hygromycin. To knock down expression of RRM2, proliferating HMECs were infected at PD 10 with lentiviral vector expressing dCas9-KRAB and sgRNA against RRM2 (forward, 5′-CACCGACACGGAGGGAGAGCATAG-3′) or nontargeting control (forward, 5′-CACCGGTATTACTGATATTGGTGGG-3′). The lentiviral vector used for CRISPRi, pLV hU6-sgRNA hUbC-dCas9-KRAB-T2a-Puro, was a gift from Charles Gersbach (Addgene plasmid 71236)

Senescence-associated β-gal measurements

HMECs were incubated with 100 nM bafilomycin A1 (Sigma-Aldrich) for 1 h to raise the lysosomal pH to 6.0 (26), followed by incubation with 33 μM C_{12}FDG (Setareh Biotech) for 1 h, lifted with TrypLE, resuspended in ice-cold PBS, and then analyzed on a Miltenyi Biotec MACSQuant flow cytometer to measure fluorescence (26). Data were processed and analyzed with FlowJo 7.6.1 software, and the mean fluorescent signal for each sample was exported. Values for SA-β-gal activity were calculated as follows: mean of samples labeled with C_{12}FDG − mean of samples without C_{12}FDG. Data were normalized to the SA-β-gal activity of nonsenescent samples.

EdU incorporation

EdU staining was performed using the Click-iT Plus EdU Alexa Fluor 594 Imaging kit (Thermo Fisher Scientific, C10639). Briefly, cells were seeded in glass bottom dishes (MatTek part number P35G-1.5-10-C) with appropriate density and then incubated with 10 μM EdU for 6 h at 37 °C. If membrane staining was desired, cells were incubated with 1× MemBrite Fix 640/660 (Biotium 30097-T) for 5 min at 37 °C. Next, cells were fixed with 3.7% formaldehyde followed by 0.5% Triton X-100 permeabilization at room temperature. Cells were incubated with Click-iT Plus reaction mixture for 30 min at room temperature protected from light. Finally, for nuclear staining, cells were incubated with 1× Hoechst 33342 for 30 min at room temperature protected from light and stored in PBS until imaging.

Confocal microscopy and cell counting

All microscopy was performed on Zeiss 780 or 880 confocal systems. The excitation wavelengths for the stained cells were: 405 nm for Hoechst, 594 nm for EdU, and 633 nm for MemBrite membrane dye (Biotium). All high-magnification images (×40/1.1 NA and ×63/1.4 NA, Zeiss) were sampled at Nyquist with 1-Airy unit pinhole diameters, and all low-magnification images (×10/0.45 NA, Zeiss) were collected with pinhole diameters such that 40-μm optical sections were obtained for cell counting. Tiled images were stitched together and analyzed using Imaris (Bitplane) image processing and analysis tools. Images were interrogated for nuclei and the presence of EdU through the Spots module in Imaris.

Mass spectrometry–based metabolomics analysis

HMECs were plated onto 6-well plates at a density of $1–3 \times 10^4$ cells/cm^2, depending on the experiment. For flux analysis, after 24 h, medium was replaced by U-^{13}C–labeled glucose, 1,2-^{13}C–labeled glucose, or U-^{13}C–labeled glutamine (Cambridge Isotope Laboratories). Metabolite extraction was performed 24 h after adding labeled medium. For extraction of intracellular metabolites, cells were washed on ice with 1 ml of ice-cold 150 mM ammonium acetate (NH_4AcO, pH 7.3). 1 ml of −80 °C cold 80% MeOH was added to the wells, samples were incubated at −80 °C for 20 min, and then cells were scraped off and supernatants were transferred into microcentrifuge tubes. Samples were pelleted at 4 °C for 5 min at 15,000 rpm. The supernatants were transferred into a LoBind Eppendorf microcentrifuge tube, the cell pellets were re-extracted with 200 μl of ice-cold 80% MeOH and spun down, and the supernatants were combined. Metabolites were dried at room temperature under vacuum and resuspended in water for the

LC-MS run. For extraction of extracellular metabolites, 20 μl of cell-free blank and conditioned medium samples were collected from wells. Metabolites were extracted by adding 500 μl of −80 °C cold 80% MeOH, dried at room temperature under vacuum, and resuspended in water for LC-MS analysis.

Samples were randomized and analyzed on a Q Exactive Plus hybrid quadrupole-Orbitrap mass spectrometer coupled to an UltiMate 3000 UHPLC system (Thermo Scientific). The mass spectrometer was run in polarity-switching mode (+3.00/−2.25 kV) with an m/z window ranging from 65 to 975. Mobile phase A was 5 mM NH_4AcO, pH 9.9, and mobile phase B was acetonitrile. Metabolites were separated on a Luna 3-μm NH_2 100-Å (150 × 2.0-mm) column (Phenomenex). The flow rate was 300 μl/min, and the gradient was from 15% A to 95% A in 18 min, followed by an isocratic step for 9 min and re-equilibration for 7 min. All samples were run in biological triplicate.

Metabolites were detected and quantified as area under the curve based on retention time and accurate mass (≤5 ppm) using TraceFinder 3.3 (Thermo Scientific) software. Raw data were corrected for naturally occurring ^{13}C abundance (60). Extracellular data were normalized to integrated cell number, which was calculated based on cell counts at the start and end of the time course and an exponential growth equation. Intracellular data were normalized to the cell number and cell volume at the time of extraction. Pathway maps were made with Cytoscape software (61).

Gene set and metabolite set enrichment analysis

For gene set expression analysis of RNA data, microarray data from HMECs (22) were compared across pairwise comparisons for stasis and pre-stasis cell cultures. Genes were then ranked by their average rank from individual experiments. RNA-Seq data from IMR90 cells (2) were ranked based on signal/noise ratio of senescent/nonsenescent cells. GSEA was run with the unweighted statistic using the GSEA java applet (40). For metabolite set enrichment analysis of metabolomic data, HMEC intracellular pool sizes or [^{13}C]glucose fractional contribution data were ranked based on $\log_2$ -fold change of senescent/proliferating, luciferase/hTERT, or triapine/DMSO. Enrichment analysis was run with unweighted statistic using the GSEA java applet.

Statistical analysis

For metabolomics data ($n = 3$ in each experiment), p value was calculated with a two-tailed Student's t test. To evaluate combined significance from independent experiments, p values were combined with Fisher's method and corrected for false discovery rate using the Benjamini–Hochberg method. For SA-β-gal activity, p values were calculated with Student's t test. For cell size analysis, p values were calculated with a Wilcox–Mann–Whitney test because the data were not normally distributed.

Immunoblot analysis

Cells were lysed in modified radioimmune precipitation assay buffer (50 mM Tris-HCl (pH 7.5), 150 mM NaCl, 50 mM β-glycerophosphate, 0.5 mM Nonidet P-40, 0.25% sodium deoxycholate, 10 mM sodium pyrophosphate, 30 mM sodium fluoride, 2 mM EDTA, 1 mM activated sodium vanadate, 20 μg/ml aprotinin, 10 μg/ml leupeptin, 1 mM DTT, and 1 mM phenylmethylsulfonyl fluoride). Whole-cell lysates were resolved by SDS-PAGE on 4–15% gradient gels and blotted onto nitrocellulose membranes (Bio-Rad). Membranes were blocked for 1 h and then incubated with primary antibodies overnight and secondary antibodies for 2 h. Blots were imaged using the Odyssey IR Imaging System (LI-COR). Primary antibodies used for Western blot analysis were as follows: p16 (10883-1-AP, Proteintech), p21 (2947S, Cell Signaling), PAI-1 (NBP1-19773, Novus Biologicals), γ-H2AX (9718S, Cell Signaling), RRM2 (103193, GeneTex; HPAA056994, Millipore Sigma), luciferase (L0159, Sigma-Aldrich), hTERT (600-401-252S, Rockland), and anti-β-actin (66009-1-Ig, Proteintech). Recombinant human p16 protein (Novus H00001029-P01) was used as a positive control for p16 Western blotting.

Author contributions—A. D. and N. G. conceived the study; A. D. performed cell culture and metabolomics experiments. S. P. and A. D. cloned lentiviral vectors for luciferase and hTERT expression. A. D., J. J., and S. F. performed and supervised immunofluorescence microscopy. A. D., J. Y., and F. S. performed Western blotting. A. D., S. L., J. M., and P. W. performed and supervised SA-β-gal activity measurements. A. D. and N. G. analyzed all data and wrote the manuscript.

References

1. Campisi, J. (2013) Aging, Cellular Senescence, and Cancer. *Annu. Rev. Physiol.* **75,** 685–705 CrossRef Medline
2. Baar, M. P., Brandt, R. M. C., Putavet, D. A., Klein, J. D. D., Derks, K. W. J., Bourgeois, B. R. M., Stryeck, S., Rijksen, Y., van Willigenburg, H., Feijtel, D. A., van der Pluijm, I., Essers, J., van Cappellen, W. A., van IJcken, W. F., Houtsmuller, A. B., *et al.* (2017) Targeted apoptosis of senescent cells restores tissue homeostasis in response to chemotoxicity and aging. *Cell* **169,** 132–147.e16 CrossRef Medline
3. Baker, D. J., Childs, B. G., Durik, M., Wijers, M. E., Sieben, C. J., Zhong, J., Saltness, R. A., Jeganathan, K. B., Verzosa, G. C., Pezeshki, A., Khazaie, K., Miller, J. D., and van Deursen, J. M. (2016) Naturally occurring p16^{Ink4a}-positive cells shorten healthy lifespan. *Nature* **530,** 184–189 CrossRef Medline
4. Jeyapalan, J. C., Ferreira, M., Sedivy, J. M., and Herbig, U. (2007) Accumulation of senescent cells in mitotic tissue of aging primates. *Mech. Ageing Dev.* **128,** 36–44 CrossRef Medline
5. Hayflick, L. (1965) The limited *in vitro* lifetime of human diploid cell strains. *Exp. Cell Res.* **37,** 614–636 CrossRef Medline
6. Aird, K. M., Zhang, G., Li, H., Tu, Z., Bitler, B. G., Garipov, A., Wu, H., Wei, Z., Wagner, S. N., Herlyn, M., and Zhang, R. (2013) Suppression of nucleotide metabolism underlies the establishment and maintenance of oncogene-induced senescence. *Cell Rep.* **3,** 1252–1265 CrossRef Medline
7. Collado, M., and Serrano, M. (2010) Senescence in tumours: evidence from mice and humans. *Nat. Rev. Cancer* **10,** 51–57 CrossRef Medline
8. Kaplon, J., Zheng, L., Meissl, K., Chaneton, B., Selivanov, V. A., Mackay, G., van der Burg, S. H., Verdegaal, E. M. E., Cascante, M., Shlomi, T., Gottlieb, E., and Peeper, D. S. (2013) A key role for mitochondrial gatekeeper pyruvate dehydrogenase in oncogene-induced senescence. *Nature* **498,** 109–112 CrossRef Medline
9. Mannava, S., Moparthy, K. C., Wheeler, L. J., Natarajan, V., Zucker, S. N., Fink, E. E., Im, M., Flanagan, S., Burhans, W. C., Zeitouni, N. C., Shewach, D. S., Mathews, C. K., and Nikiforov, M. A. (2013) Depletion of deoxyribonucleotide pools is an endogenous source of DNA damage in cells undergoing oncogene-induced senescence. *Am. J. Pathol.* **182,** 142–151 CrossRef Medline

10. Coppé, J.-P., Desprez, P.-Y., Krtolica, A., and Campisi, J. (2010) The senescence-associated secretory phenotype: the dark side of tumor suppression. *Annu. Rev. Pathol.* **5,** 99–118 CrossRef Medline
11. Wiley, C. D., and Campisi, J. (2016) From ancient pathways to aging cells—connecting metabolism and cellular senescence. *Cell Metab.* **23,** 1013–1021 CrossRef Medline
12. Bittles, A. H., and Harper, N. (1984) Increased glycolysis in ageing cultured human diploid fibroblasts. *Biosci. Rep.* **4,** 751–756 CrossRef Medline
13. James, E. L., Michalek, R. D., Pitiyage, G. N., de Castro, A. M., Vignola, K. S., Jones, J., Mohney, R. P., Karoly, E. D., Prime, S. S., and Parkinson, E. K. (2015) Senescent human fibroblasts show increased glycolysis and redox homeostasis with extracellular metabolomes that overlap with those of irreparable DNA damage, aging, and disease. *J. Proteome Res.* **14,** 1854–1871 CrossRef Medline
14. Zwerschke, W., Mazurek, S., Stöckl, P., Hütter, E., Eigenbrodt, E., and Jansen-Dürr, P. (2003) Metabolic analysis of senescent human fibroblasts reveals a role for AMP in cellular senescence. *Biochem. J.* **376,** 403–411 CrossRef Medline
15. Li, M., Durbin, K. R., Sweet, S. M. M., Tipton, J. D., Zheng, Y., and Kelleher, N. L. (2013) Oncogene-induced cellular senescence elicits an anti-Warburg effect. *Proteomics* **13,** 2585–2596 CrossRef Medline
16. Mazurek, S., Zwerschke, W., Jansen-Dürr, P., and Eigenbrodt, E. (2001) Metabolic cooperation between different oncogenes during cell transformation: interaction between activated ras and HPV-16 E7. *Oncogene* **20,** 6891–6898 CrossRef Medline
17. Moiseeva, O., Bourdeau, V., Roux, A., Deschênes-Simard, X., and Ferbeyre, G. (2009) Mitochondrial dysfunction contributes to oncogene-induced senescence. *Mol. Cell. Biol.* **29,** 4495–4507 CrossRef Medline
18. Wiley, C. D., Velarde, M. C., Lecot, P., Liu, S., Sarnoski, E. A., Freund, A., Shirakawa, K., Lim, H. W., Davis, S. S., Ramanathan, A., Gerencser, A. A., Verdin, E., and Campisi, J. (2016) Mitochondrial dysfunction induces senescence with a distinct secretory phenotype. *Cell Metab.* **23,** 303–314 CrossRef Medline
19. Jiang, P., Du, W., Mancuso, A., Wellen, K. E., and Yang, X. (2013) Reciprocal regulation of p53 and malic enzymes modulates metabolism and senescence. *Nature* **493,** 689–693 CrossRef Medline
20. Kondoh, H., Lleonart, M. E., Gil, J., Wang, J., Degan, P., Peters, G., Martinez, D., Carnero, A., and Beach, D. (2005) Glycolytic enzymes can modulate cellular life span. *Cancer Res.* **65,** 177–185 Medline
21. Stampfer, M. R., LaBarge, M. A., and Garbe, J. C. (2013) An integrated human mammary epithelial cell culture system for studying carcinogenesis and aging. in *Cell and Molecular Biology of Breast Cancer*, pp. 323–361, Humana Press, Totowa, NJ
22. Garbe, J. C., Bhattacharya, S., Merchant, B., Bassett, E., Swisshelm, K., Feiler, H. S., Wyrobek, A. J., and Stampfer, M. R. (2009) Molecular distinctions between the stasis and telomere attrition senescence barriers demonstrated by long-term culture of normal human mammary epithelial cells. *Cancer Res.* **69,** 7557–7568 CrossRef Medline
23. Garbe, J. C., Holst, C. R., Bassett, E., Tlsty, T., and Stampfer, M. R. (2007) Inactivation of p53 function in cultured human mammary epithelial cells turns the telomere-length dependent senescence barrier from agonescence into crisis. *Cell Cycle* **6,** 1927–1936 CrossRef Medline
24. Romanov, S. R., Kozakiewicz, B. K., Holst, C. R., Stampfer, M. R., Haupt, L. M., and Tlsty, T. D. (2001) Normal human mammary epithelial cells spontaneously escape senescence and acquire genomic changes. *Nature* **409,** 633–637 CrossRef Medline
25. Chen, Q. M., Tu, V. C., Catania, J., Burton, M., Toussaint, O., and Dilley, T. (2000) Involvement of Rb family proteins, focal adhesion proteins and protein synthesis in senescent morphogenesis induced by hydrogen peroxide. *J. Cell Sci.* **113,** 4087–4097 Medline
26. Debacq-Chainiaux, F., Erusalimsky, J. D., Campisi, J., and Toussaint, O. (2009) Protocols to detect senescence-associated beta-galactosidase (SA-βgal) activity, a biomarker of senescent cells in culture and *in vivo*. *Nat. Protoc.* **4,** 1798–1806 CrossRef Medline
27. Kosar, M., Bartkova, J., Hubackova, S., Hodny, Z., Lukas, J., and Bartek, J. (2011) Senescence-associated heterochromatin foci are dispensable for cellular senescence, occur in a cell type- and insult-dependent manner and follow expression of p16(ink4a). *Cell Cycle* **10,** 457–468 CrossRef Medline
28. Leikam, C., Hufnagel, A. L., Otto, C., Murphy, D. J., Mühling, B., Kneitz, S., Nanda, I., Schmid, M., Wagner, T. U., Haferkamp, S., Bröcker, E.-B., Schartl, M., and Meierjohann, S. (2015) *In vitro* evidence for senescent multinucleated melanocytes as a source for tumor-initiating cells. *Cell Death Dis.* **6,** e1711 CrossRef Medline
29. Dikovskaya, D., Cole, J. J., Mason, S. M., Nixon, C., Karim, S. A., McGarry, L., Clark, W., Hewitt, R. N., Sammons, M. A., Zhu, J., Athineos, D., Leach, J. D. G., Marchesi, F., van Tuyn, J., Tait, S. W., *et al.* (2015) Mitotic stress is an integral part of the oncogene-induced senescence program that promotes multinucleation and cell cycle arrest. *Cell Rep.* **12,** 1483–1496 CrossRef Medline
30. Herbig, U., Jobling, W. A., Chen, B. P. C., Chen, D. J., and Sedivy, J. M. (2004) Telomere shortening triggers senescence of human cells through a pathway involving ATM, p53, and p21CIP1, but not p16INK4a. *Mol. Cell.* **14,** 501–513 CrossRef Medline
31. Vaughan, D. E., Rai, R., Khan, S. S., Eren, M., and Ghosh, A. K. (2017) Plasminogen activator inhibitor-1 is a marker and a mediator of senescence. *Arterioscler. Thromb. Vasc. Biol.* **37,** 1446–1452 CrossRef Medline
32. Eren, M., Boe, A. E., Klyachko, E. A., and Vaughan, D. E. (2014) Role of plasminogen activator inhibitor-1 in senescence and aging. *Semin. Thromb. Hemost.* **40,** 645–651 CrossRef Medline
33. Kortlever, R. M., Higgins, P. J., and Bernards, R. (2006) Plasminogen activator inhibitor-1 is a critical downstream target of p53 in the induction of replicative senescence. *Nat. Cell Biol.* **8,** 877–884 CrossRef Medline
34. Graham, N. A., Minasyan, A., Lomova, A., Cass, A., Balanis, N. G., Friedman, M., Chan, S., Zhao, S., Delgado, A., Go, J., Beck, L., Hurtz, C., Ng, C., Qiao, R., Ten Hoeve, J., *et al.* (2017) Recurrent patterns of DNA copy number alterations in tumors reflect metabolic selection pressures. *Mol. Syst. Biol.* **13,** 914 CrossRef Medline
35. Yuan, M., Breitkopf, S. B., Yang, X., and Asara, J. M. (2012) A positive/negative ion-switching, targeted mass spectrometry-based metabolomics platform for bodily fluids, cells, and fresh and fixed tissue. *Nat. Protoc.* **7,** 872–881 CrossRef Medline
36. Wang, W., Yang, X., López de Silanes I., Carling, D., and Gorospe, M. (2003) Increased AMP:ATP ratio and AMP-activated protein kinase activity during cellular senescence linked to reduced HuR function. *J. Biol. Chem.* **278,** 27016–27023 CrossRef Medline
37. Jang, C., Chen, L., and Rabinowitz, J. D. (2018) Metabolomics and isotope tracing. *Cell* **173,** 822–837 CrossRef Medline
38. Buescher, J. M., Antoniewicz, M. R., Boros, L. G., Burgess, S. C., Brunengraber, H., Clish, C. B., DeBerardinis, R. J., Feron, O., Frezza, C., Ghesquiere, B., Gottlieb, E., Hiller, K., Jones, R. G., Kamphorst, J. J., Kibbey, R. G., *et al.* (2015) A roadmap for interpreting ^{13}C metabolite labeling patterns from cells. *Curr. Opin. Biotechnol.* **34,** 189–201 CrossRef Medline
39. Metallo, C. M., Walther, J. L., and Stephanopoulos, G. (2009) Evaluation of ^{13}C isotopic tracers for metabolic flux analysis in mammalian cells. *J. Biotechnol.* **144,** 167–174 CrossRef Medline
40. Subramanian, A., Tamayo, P., Mootha, V. K., Mukherjee, S., Ebert, B. L., Gillette, M. A., Paulovich, A., Pomeroy, S. L., Golub, T. R., Lander, E. S., and Mesirov, J. P. (2005) Gene set enrichment analysis: a knowledge-based approach for interpreting genome-wide expression profiles. *Proc. Natl. Acad. Sci.* **102,** 15545–15550 CrossRef Medline
41. Kanehisa, M., Goto, S., Sato, Y., Kawashima, M., Furumichi, M., and Tanabe, M. (2014) Data, information, knowledge and principle: back to metabolism in KEGG. *Nucleic Acids Res.* **42,** D199–D205 CrossRef Medline
42. Garbe, J. C., Vrba, L., Sputova, K., Fuchs, L., Novak, P., Brothman, A. R., Jackson, M., Chin, K., LaBarge, M. A., Watts, G., Futscher, B. W., and Stampfer, M. R. (2014) Immortalization of normal human mammary epithelial cells in two steps by direct targeting of senescence barriers does not require gross genomic alterations. *Cell Cycle* **13,** 3423–3435 CrossRef Medline
43. Popović-Bijelić, A., Kowol, C. R., Lind, M. E. S., Luo, J., Himo, F., Enyedy, E. A., Arion, V. B., and Gräslund, A. (2011) Ribonucleotide reductase inhibition by metal complexes of Triapine (3-aminopyridine-2-carboxaldehyde thiosemicarbazone): a combined experimental and theoretical study. *J. Inorg. Biochem.* **105,** 1422–1431 CrossRef Medline

44. Thakore, P. I., D'Ippolito, A. M., Song, L., Safi, A., Shivakumar, N. K., Kabadi, A. M., Reddy, T. E., Crawford, G. E., and Gersbach, C. A. (2015) Highly specific epigenome editing by CRISPR-Cas9 repressors for silencing of distal regulatory elements. *Nat. Methods* **12,** 1143–1149 CrossRef Medline
45. Aye, Y., Li, M., Long, M. J. C., and Weiss, R. S. (2015) Ribonucleotide reductase and cancer: biological mechanisms and targeted therapies. *Oncogene* **34,** 2011–2021 CrossRef Medline
46. Pai, C.-C., and Kearsey, S. E. (2017) A critical balance: dNTPs and the maintenance of genome stability. *Genes* (*Basel*) **8,** E57 CrossRef Medline
47. Kumar, D., Abdulovic, A. L., Viberg, J., Nilsson, A. K., Kunkel, T. A., and Chabes, A. (2011) Mechanisms of mutagenesis *in vivo* due to imbalanced dNTP pools. *Nucleic Acids Res.* **39,** 1360–1371 CrossRef Medline
48. Lamm, N., Maoz, K., Bester, A. C., Im, M. M., Shewach, D. S., Karni, R., and Kerem, B. (2015) Folate levels modulate oncogene-induced replication stress and tumorigenicity. *EMBO Mol. Med.* **7,** 1138–1152 CrossRef Medline
49. Bester, A. C., Roniger, M., Oren, Y. S., Im, M. M., Sarni, D., Chaoat, M., Bensimon, A., Zamir, G., Shewach, D. S., and Kerem, B. (2011) Nucleotide deficiency promotes genomic instability in early stages of cancer development. *Cell* **145,** 435–446 CrossRef Medline
50. Hsu, C.-W., Chen, Y.-C., Su, H.-H., Huang, G.-J., Shu, C.-W., Wu, T. T.-L., and Pan, H.-W. (2017) Targeting TPX2 suppresses the tumorigenesis of hepatocellular carcinoma cells resulting in arrested mitotic phase progression and increased genomic instability. *J. Cancer* **8,** 1378–1394 CrossRef Medline
51. Knecht, H., Sawan, B., Lichtensztejn, D., Lemieux, B., Wellinger, R. J., and Mai, S. (2009) The 3D nuclear organization of telomeres marks the transition from Hodgkin to Reed–Sternberg cells. *Leukemia* **23,** 565–573 CrossRef Medline
52. Mirzayans, R., Andrais, B., and Murray, D. (2018) Roles of polyploid/multinucleated giant cancer cells in metastasis and disease relapse following anticancer treatment. *Cancers* (*Basel*) **10,** E118 CrossRef Medline
53. Aird, K. M., Worth, A. J., Snyder, N. W., Lee, J. V., Sivanand, S., Liu, Q., Blair, I. A., Wellen, K. E., and Zhang, R. (2015) ATM couples replication stress and metabolic reprogramming during cellular senescence. *Cell Rep.* **11,** 893–901 CrossRef Medline
54. Foskolou, I. P., Jorgensen, C., Leszczynska, K. B., Olcina, M. M., Tarhonskaya, H., Haisma, B., D'Angiolella, V., Myers, W. K., Domene, C., Flashman, E., and Hammond, E. M. (2017) Ribonucleotide reductase requires subunit switching in hypoxia to maintain DNA replication. *Mol. Cell.* **66,** 206–220.e9 CrossRef Medline
55. Kuo, M.-L., Sy, A. J., Xue, L., Chi, M., Lee, M. T.-C., Yen, T., Chiang, M.-I., Chang, L., Chu, P., and Yen, Y. (2012) RRM2B suppresses activation of the oxidative stress pathway and is up-regulated by p53 during senescence. *Sci. Rep.* **2,** 822 CrossRef Medline
56. Cordes, T., and Metallo, C. M. (2016) Tracing insights into human metabolism using chemical engineering approaches. *Curr. Opin. Chem. Eng.* **14,** 72–81 CrossRef Medline
57. Ben-Sahra, I., Howell, J. J., Asara, J. M., and Manning, B. D. (2013) Stimulation of *de novo* pyrimidine synthesis by growth signaling through mTOR and S6K1. *Science* **339,** 1323–1328 CrossRef Medline
58. Kim, J., Hu, Z., Cai, L., Li, K., Choi, E., Faubert, B., Bezwada, D., Rodriguez-Canales, J., Villalobos, P., Lin, Y.-F., Ni, M., Huffman, K. E., Girard, L., Byers, L. A., Unsal-Kacmaz, K., *et al.* (2017) CPS1 maintains pyrimidine pools and DNA synthesis in KRAS/LKB1-mutant lung cancer cells. *Nature* **546,** 168–172 CrossRef Medline
59. Dörr, J. R., Yu, Y., Milanovic, M., Beuster, G., Zasada, C., Däbritz, J. H. M., Lisec, J., Lenze, D., Gerhardt, A., Schleicher, K., Kratzat, S., Purfürst, B., Walenta, S., Mueller-Klieser, W., Gräler, M., *et al.* (2013) Synthetic lethal metabolic targeting of cellular senescence in cancer therapy. *Nature* **501,** 421–425 CrossRef Medline
60. Moseley, H. N. (2010) Correcting for the effects of natural abundance in stable isotope resolved metabolomics experiments involving ultra-high resolution mass spectrometry. *BMC Bioinformatics* **11,** 139 CrossRef Medline
61. Shannon, P., Markiel, A., Ozier, O., Baliga, N. S., Wang, J. T., Ramage, D., Amin, N., Schwikowski, B., and Ideker, T. (2003) Cytoscape: a software environment for integrated models of biomolecular interaction networks. *Genome Res.* **13,** 2498–2504 CrossRef Medline